Numerical investigation of the coupled aero-hydrodynamic performances of a semi-submersible floating offshore wind turbine with inclined columns

Ying-jie Xue[1], Xiao-long Yang[2], Wei-wen Zhao[1], De-cheng Wan[1*]
1. *Computational Marine Hydrodynamics Lab (CMHL), School of Naval Architecture, Ocean and Civil Engineering, Shanghai Jiao Tong University, Shanghai 200240, China*
2. *Offshore Oil Engineering Co. Ltd., Tianjin 300461, China*

Abstract: Numerical investigations of floating platforms with different outer column inclined angles under two operating conditions of regular wave and irregular wave are presented in this paper. A coupled aero-hydrodynamic computational fluid dynamics in-house solver FOWT-UALM-SJTU is applied for the calculation. First, the validation for wave and wind generation are conducted to determine mesh distribution strategy. Based on these, the hydrodynamic motion response, aerodynamic performance and wake flow are analyzed to explore the impact of inclined angle. Conduct spectral analysis on the motion response under wave action, discuss the aerodynamic attack angle and inflow wind velocity along the blade spanwise direction in detail, reveal different trends in wake development and recovery. The results show that for the regular wave condition with the increase of inclined angles, the equilibrium position of surge motion is constantly rising, while pitch is decreasing. The maximum root mean square (rms) value occurs at angle = 30°, compared with the original OC4 FOWT, the rms in power and thrust increase 0.35%, 0.71%. And there are two low regions of attack angle and high regions of axial inflow velocity, corresponding to aerodynamic loads. The spectral analysis indicates that the natural frequency of pitch motion will increase with inclined angle. Besides, from the middle to far region of wake flow, the velocity recovery of FOWT with inclined angle will become faster, which is beneficial for downstream turbines to enhance more wind energy.

Key words: Floating offshore wind turbine, numerical simulation, aero-hydrodynamic coupled analysis, floating platform with inclined columns, wake flow recovery

0. Introduction

Since the beginning of the 21st-Century, with the energy crisis gradually intensifying, in the near future the fossil energy will not be able to meet human needs. Therefore, countries around the world are expanding the development and utilization of the new energy resources, including solar energy, nuclear energy, ocean energy, wind energy, biomass energy, etc. Among these, the wind energy resources have large reserves and wide distribution, besides it will never be depleted[1-2]. Especially, because the ocean occupies 71% of the earth surface, there are bigger free areas for installations compared with onshore. Also, the offshore wind energy has a broad development prospect benefiting from its higher wind speed, lower turbulent effects, far from population areas and less visual and noise pollution[3-4]. According to Global Wind Energy Council's report[5] in 2023, from 2002 to 2022, the total installations of offshore wind turbines has grown to 64 GW, accounting for 7% of the total. Only in the past two years, the newly installed capacity has reached up to 29.9 GW. They expect that there will be 680GW of wind capacity installed globally by 2027, of which 130 GW will be offshore.

With the increasing scales of turbine blades and the continuous development of deep seas[6], they will face more complex and severe environmental conditions which put forward some new requirements for stability of floating offshore wind turbine (FOWT) platform[7]. Therefore, it is necessary to conduct research on the structural optimization design of FOWT platform.

In early studies, parametric design and modeling is a common method. Within the restricted space, variation parameters should cut across a wide range of the semi-submersible platform types or styles[8]. While, due to the complex dynamic behaviors of FOWT system, the multidisciplinary design analysis and

optimization (MADO) technique was used which is transplanted from aerospace industry. Focusing on the hydrodynamic response amplitude operator (RAO) of platform, Sclavounos et al.[9], Tracy[10] presented a coupled dynamic analysis of floating wind turbines incorporating the parametric research for the platform draft and column diameter. Combing with the analysis of nacelle acceleration, mooring tension, and displacement, the Pareto optimal results point to a spar which has a narrow deep draft and a shallow drafted barge ballasted with concrete. A coupled of FAST and AQWA[11] was used by Zou et al.[12] to calculate the time domain response of 5 MW FOWT platform under multiple environmental conditions, and the approximate prediction model for response was established based on Kriging technique and multiple-objective genetic algorithm method. The approximate response surface prediction model of the optimal platform shows well prediction on a rough ocean condition. Considering the mooring line, Brommundt et al.[13] presented an optimal layout method to minimum the mooring costs. And the effect of mooring line damping on the dynamic behaviors of the conceptual FOWT were studied by Zhao et al.[14] After optimization, the platform which is supporting Technical University of Denmark (DTU) 10 MW wind turbine performs well being tested under various operating and fault conditions, including blade seize with or without shutdown. Aiming at the 15 MW FOWT semi-submersible platform VolturnUS-S, Liu et al.[15] optimized the distance and diameter of outer columns. It is indicated that 33.61% of pitch peak value decreases while increasing the column spacing 5% for the optimal foundation type. When the installation cost and wind turbine power are concerned, there are nine variable parameters, optimization of which performed by Karimi et al.[16], including inner cylinder draft, inner cylinder radius, top taper ratio etc. Taking the root mean square (rms) of nacelle acceleration and structural cost as optimization objectives based on the genetic algorithm, optimization research was conducted on the number of columns and the size of the heave plate[17]. It is advised that three outer columns are best below a cost of 6×10^6, six outer columns are best above a cost of 6×10^6. And the heavy plate size should increase with the cost. Besides, attention has also been paid to structural fatigue or other aspects. In Hegseth et al.[18] research, a MADO technique was adopted, and the constrains have been placed on the fatigue (FLS) and ultimate (ULS) limit state calculated by SN curves and Dirlik method[19]. Their objective function focused on the cost and power quality which aims to optimize spar column diameter and wall thickness.

A semi-submersible FOWT platform named OC4[20] which is designed as a foundation of National Renewable Energy Laboratory (NREL) 5 MW wind turbine[21] has become more popular around the researchers[22-24], due to the detailed hydrodynamic data provided in their design report. Try to support DTU 10 MW wind turbine, the parameters of draft, outer column radius and column spacing of OC4 platform were enlarged by Ferri et al.[25-26]. The model after optimization could reduce the RAO peak of heave and pitch 54% and 50% respectively. Liu et al.[27] divided each mooring line into three sections, studied the effect of sections length for RAO response. Besides, under complex regular and irregular wave conditions, the outer columns with different inclined angle are calculated by their in-house code based on potential theory, which shows that the angle of inclined column could reduce heave and pitch motion effectively. Zhang et al.[28] proposed a new platform with inclined side columns referring from OC4 and OC3 spar platform. The new foundation model could interface rougher wave conditions.

Although there are more studies and researches focusing on the optimization, their numerical methods are mostly based on potential method. Some of them only conducted the frequency analysis. Before that, we have conducted hydrodynamic analysis for 3 types FOWT with different inclined angles of outer column not considering the aerodynamic force of the wind turbine[29]. The results indicate that increasing angle could reduce pitch motion amplitude. In this article, a coupled areo-hydrodynamic in-house solver FOWT-UALM-SJTU is used for integrated performance analysis to discuss the impact of different inclined column angles on hydro-aero dynamic performance and wake flow.

1. Numerical methods

In this study, we utilize our in-house computational fluid dynamics solver FOWT-UALM-SJTU[30-31] which is based on the open-source software OpenFOAM. It was employed to solve coupled aero- hydrodynamic problems. The aerodynamic module adopts actuator line model (ALM). The hydrodynamic calculation module, derived from our in-house solver naoe-FOAM-SJTU[32], is capable of solving the six degrees of freedom (6DOF) motion response of a floating body. The mooring calculation module employs the piecewise extrapolating method (PEM) for calculating the tension of anchor chain[33-34].

1.1 Governing equations

The Navier-Stokes (N-S) equation is the governing equation of fluid mechanics. It consists of the continuity equation and momentum equation two parts. For the incompressible problems, they are expressed as

$$\nabla \cdot \boldsymbol{U} = 0 \tag{1}$$

$$\frac{\partial \rho \boldsymbol{U}}{\partial t} + \nabla \cdot (\rho \boldsymbol{U}\boldsymbol{U}) = -\nabla p_{\mathrm{d}} - \boldsymbol{g}\cdot \boldsymbol{x}\,\nabla\rho + \nabla \cdot (\mu \cdot \nabla\boldsymbol{U})$$

$$(2)$$

where $\boldsymbol{U}$ is the velocity of flow field, ρ is the density of the fluid (water), $\boldsymbol{x}$ is the Cartesian coordinate vector (x, y, z), p_{d} is the dynamic pressure, $\boldsymbol{g}$ is the gravity field, μ is the dynamic viscosity coefficient of the water. In this study, the DDES-SST[35-36] turbulent model is used for simulation.

1.2 *Volume of fluid model*

The volume of fluid method was proposed by Hirt and Nichols[37] which is a two-phase flow method used to capture the free surface. The transport equation like this

$$\frac{\partial \alpha_{\mathrm{v}}}{\partial t} + \nabla \cdot (\alpha_{\mathrm{v}}\boldsymbol{U}) = 0 \qquad (3)$$

where α_{v} is the volume fraction, in air, $\alpha_{\mathrm{v}} = 0$, in water, $\alpha_{\mathrm{v}} = 1$, and near the free surface, $0 < \alpha_{\mathrm{v}} < 1$.

A surface tension source term f_{σ} would be added into N-S equation.

$$f_{\sigma} = \sigma\kappa\nabla\alpha_{\mathrm{v}} \qquad (4)$$

where σ is the surface tension, κ is the curvature of surface interface.

1.3 *Wave generation and absorption module*

In our solver, the wave is generated by defining the volume fraction and field velocity at the inlet boundary. In this paper, the regular wave generated by fifth-order Stokes wave theory, and the irregular wave is based on JONSWAP wave spectrum.

Fifth-order Stokes wave theory defines the wave surface function[38]

$$\eta(\boldsymbol{x},t) = \frac{1}{|\boldsymbol{k}|}\sum_{n=1}^{5} S_n\cos(n\boldsymbol{k}\cdot\boldsymbol{x} - \omega t + \varphi) \qquad (5)$$

where $\boldsymbol{k}$ is the wave number, considering wave direction, ω is the wave circular frequency, φ is the wave phase. The coefficient S_n is taken from Fenton's[38] paper.

The irregular wave spectrum defines the wave surface function

$$\eta(\boldsymbol{x},t) = \sum_{i=1}^{N_f} a_i\cos(\boldsymbol{k}_i\cdot\boldsymbol{x} - \omega_i t + \varphi_i) \qquad (6)$$

where N_f is the number of wave components, subscript i is the i-th wave component, $\boldsymbol{k}_i$ and ω_i are the wave number and circular frequency. The wave amplitude a_i could be calculated by energy density $S(f)$

$$a_i = \sqrt{2S(f_i)\Delta f} \qquad (7)$$

where f is the frequency, Δf is the frequency spacing. In JONSWAP wave spectrum:

$$S(f) = \frac{319.34}{(2\pi)^4}\frac{H_{\mathrm{s}}^2 f_{\mathrm{p}}^4}{f^5}\gamma^{\beta}\mathrm{e}^{(-5/4)(f_{\mathrm{p}}^4/f^4)},$$

$$\beta = \mathrm{e}^{[-(f-f_{\mathrm{p}})^2]/(2\sigma^2 f_{\mathrm{p}}^2)} \qquad (8)$$

where H_{s} is the significant wave height, f_{p} is the spectral peak frequency.

The sponge layer is set near the end of outlet boundary to reduce reflection. The absorption source term can be described like this:

$$f_{\mathrm{S}}(x) = -\rho\alpha_{\mathrm{S}}\left(\frac{\boldsymbol{x} - \boldsymbol{x}_{\mathrm{S}}}{L_{\mathrm{S}}}\right)^2 \boldsymbol{U} \quad \text{inside sponge layer}$$

$$(9a)$$

$$f_{\mathrm{S}}(x) = 0 \quad \text{outside sponge layer} \qquad (9b)$$

where α_{S} is custom viscosity parameter, L_{S} is the length of sponge layer and $\boldsymbol{x}_{\mathrm{S}}$ is location of damping zone start point in the wave tank.

1.4 *Aerodynamic calculation*

The actuator line model (ALM) was proposed by Sørensen and Shen[39], which is a simplified simulation method for calculating the aerodynamic of wind turbine. The basic idea is to discretize an entire turbine blade into a set of blade element units, and the blade is treated as a rotating line. Each blade element is represented by an actuator point as Fig. 1.

Based on the blade element theory, the aerodynamic force of per unit length is

$$\boldsymbol{f} = (\boldsymbol{L},\boldsymbol{D}) = 0.5\rho\boldsymbol{U}_{\mathrm{rel}}^2 c N_{\mathrm{b}}(C_{\mathrm{L}}\boldsymbol{e}_{\mathrm{L}} + C_{\mathrm{D}}\boldsymbol{e}_{\mathrm{D}}) \qquad (10)$$

where $\boldsymbol{L}$ and $\boldsymbol{D}$ represent the lift and drag force of airfoil section in two dimensions, $\boldsymbol{U}_{\mathrm{rel}}$ is the relative wind velocity at the airfoil section, c is the chord length of the airfoil section, N_{b} is the number of wind

turbine blades. C_L and C_D are the lift and drag coefficient, $\boldsymbol{e}_L$ and $\boldsymbol{e}_D$ are the unit vector in x- and y-direction in the body coordinate system.
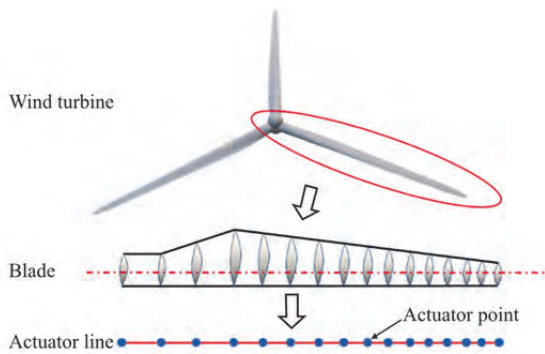

Fig. 1 (Color online) Actuator line model and actuator point

Considering platform's motion, improve the traditional ALM method to unsteady ALM (UALM) method, where $\boldsymbol{U}_{\text{rel}}$ can be expressed as

$$\boldsymbol{U}_{\text{rel}} = \boldsymbol{U}_{\text{wind}} + \boldsymbol{U}_{\text{B}} + \boldsymbol{U}_{\text{M}} \tag{11}$$

where $\boldsymbol{U}_{\text{wind}}$ the is the wind velocity in air, $\boldsymbol{U}_{\text{B}}$ is the blade rotating velocity, $\boldsymbol{U}_{\text{M}}$ is the velocity caused by platform motion. The relationship among all of them shows in Fig. 2.
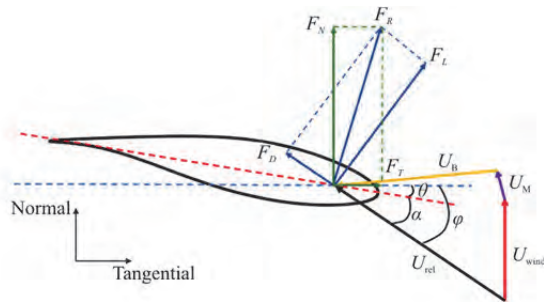

Fig. 2 (Color online) Airfoil section element

As a force source term, $\boldsymbol{f}$ will be projected into the fluid field. The Gaussian kernel function $\eta_\varepsilon(d_i)$ is used to smooth, and project the body force of each actuator point onto the grid nodes in the fluid field.

$$\boldsymbol{f}_\varepsilon(x, y, z) = \sum_{i=1}^{N_p} \boldsymbol{f}(x_i, y_i, z_i)\eta_\varepsilon(d_i) \tag{12}$$

where d_i is distance between the grid node position and the actuator point. $\eta_\varepsilon(d_i)$ could be expressed as

$$\eta_\varepsilon(d_i) = \frac{1}{\varepsilon^3 \pi^{3/2}} \exp\left[-\frac{(x_i - x)^2 + (y_i - y)^2 + (z_i - z)^2}{\varepsilon^2}\right] \tag{13}$$

where ε is the Gaussian distribution width coefficient.

For numerical simulation, incorporate the aerodynamic body force after smoothing into N-S equation. Besides, considering the surface tension and absorption source terms, the N-S equation could be expressed like this

$$\frac{\partial \rho \boldsymbol{U}}{\partial t} + \nabla \cdot (\rho \boldsymbol{U} \boldsymbol{U}) = -\nabla p_d - \boldsymbol{g} x \nabla \rho +$$

$$\nabla \cdot (\mu \nabla \boldsymbol{U}) + f_\sigma + f_S + f_\varepsilon \tag{14}$$

1.5 Hydrodynamic calculation

In our solver, the hydrodynamic 6DOF motion module is developed based on Euler angle description. There are two coordinate system, earth-fixed and ship-fixed employed into calculate rigid body motion. The turbine force and torque will be induced in calculation.

1.6 Mooring tension

Piecewise extrapolating method divides the entire mooring line into multiple cable segments. The calculation result is extrapolated from the previous cable segment to the next cable segment, as shown in Fig. 3. Equation is as follow:

$$T_{xi+1} - T_{xi} - F_i ds \cos\varphi_{i+1} - D_i ds \sin\varphi_{i+1} = \rho g A \Delta z' \cos\varphi_{i+1},$$

$$T_{zi+1} - T_{zi} - F_i ds \sin\varphi_{i+1} - D_i ds \cos\varphi_{i+1} = \rho g A \Delta z' \sin\varphi_{i+1} \tag{15}$$

where the subscript i is the i-th cable segment, T_x and T_z are the mooring tension in horizontal and vertical direction, D and F are normal and tangential hydrodynamic components per unit length of the segment, which calculated by Morison equation as Eq. (16), ds is the cable segment length, A is the area of cable section, φ indicates the angle between the cable segments and the horizontal direction and Δz is the vertical distance between the upper and lower nodes of the cable segment.

$$D_i = \frac{1}{2}\rho C_{D,n} D U_n^2, \quad F_i = \frac{1}{2}\rho C_{D,t}(\pi D)U_t^2 \tag{16}$$

where $C_{D,n}$ and $C_{D,t}$ are the drag coefficient in nor-

mal and tangential direction, U_n and U_t are the velocity components of the fluid field velocity at the cable segment.
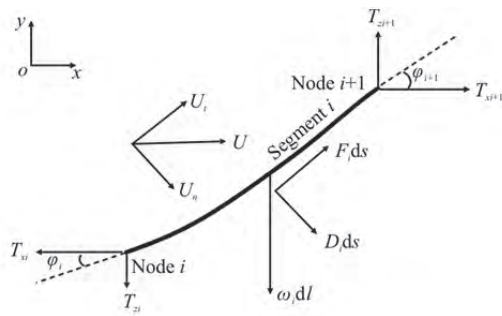

Fig. 3 (Color online) Analysis of mooring forces at the cable segment

All in all, the coupled of aero-hydrodynamic framework is shown in Fig. 4.
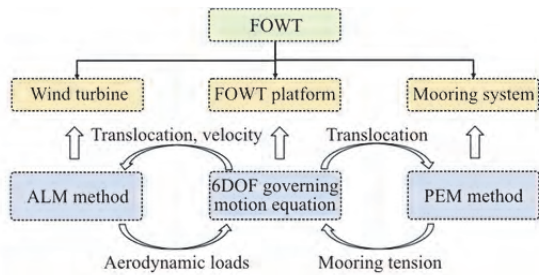

Fig. 4 (Color online) Coupling effects between the wind turbine, floating platform, and mooring system

2. Simulation condition

2.1 Original OC4 FOWT model

2.1.1 OC4 platform model

Multiple physical parameters such as geometric mass, moment of inertia, light weight information, ballast water etc. are provided in detail in report[20]. The model is shown in the Fig. 5.
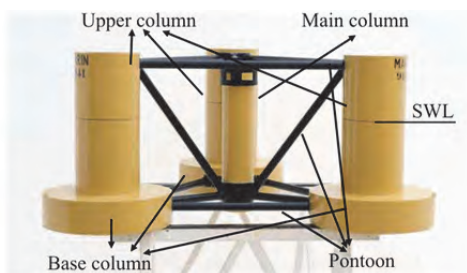

Fig. 5 (Color online) OC4 FOWT platform model[20, 29]

The walls steal thicknesses of different structural components have been also provided. For main column,

upper column, base column and pontoon, the thicknesses are 0.03 m, 0.06 m, 0.06 m and 0.0175 m. And the density of wall steal plate is 7 850 kg/m^3. Thus, the structure mass will be calculated, as shown in Table 1. The CoM means center of mass. Besides, the ballast water is distributed in the upper column and base column as Fig. 6.
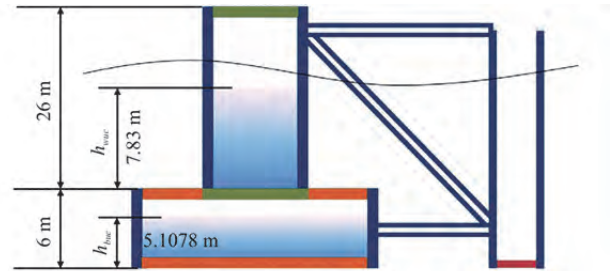

Fig. 6 (Color online) Ballast water[20, 29]

Table 1 OC4 properties[20]

Properties	Value
Light mass/10^{6}kg	3.85218
CoM location bellow SWL/m	−8.6588
Roll inertia about CoM (I_{xx}) /10^{9}kg·m^2	2.56193
Pitch inertia about CoM (I_{yy}) /10^{9}kg·m^2	2.56193
Yaw inertia about CoM (I_{zz}) /10^{9}kg·m^2	4.24260
Ballast water mass/10^{6}kg	9.62080
Platform mass, with ballast/10^{6}kg	13.4730
CoM location bellow SWL (including ballast)/m	−13.46
Moment of inertia, with ballast (I_{xx}, I_{yy}, I_{zz}) /10^{9}kg·m^2	(6.827, 6.827, 12. 26)

2.1.2 NREL 5MW wind turbine model

NREL 5MW wind turbine has 3 turbine blades, and the diameter of rotor disk is 126 m. Other parameters are listed in Table 2.

Table 2 NREL 5MW wind turbin[21]

Turbine properties	Value
Rated power/MW	5
Rotor, hub diameter/m	126, 3
Hub, tower[1] height/m	90.0, 87.6
Rated, cut-in, cut-out wind speed/(m·s^{-1})	11.4, 3.0, 25.0
Rated, cut-in rotor speed/rpm	6.9, 12.1
Rated tip speed/(m·s^{-1})	80
Overhang/m	5
Shaft tilt, precone/°	5.0, 2.5
Rotor mass/kg	110 000
Nacelle mass/kg	240 000
Tower mass/kg	347 460
CoM position[2]/m^2	(−0.2362, 0, 70.2550)

Note: [1]Tower height take into account 10 m exceeding height for OC4 platform main column above free surface. [2]Calculate from Jonkman et al.[21] report.

2.1.3 Mooring line

The positions of fairlead points and anchor points

won't change when model with different inclined angles. The initial properties are listed in Table 3.

Table 3 Mooring properties for OC4 FOWT[20]

Mooring properties	Value
Depth to anchors below SWL/m	200
Depth to fairleads below SWL/m	14
Radius to anchors from platform centerline/m	837.6
Radius to fairleads from platform centerline/m	40.868
Unstretched mooring line length/m	835.5
Volume equivalent diameter/m	0.0766
Equivalent mooring line mass density/kg·m^{-1}	113.35
Equivalent mooring line mass in water/ kg·m^{-1}	108.63
Equivalent mooring line extensional stiffness/MN	753.6
Hydrodynamic drag and added-mass coefficient for mooring lines	1.1,1.0

2.1.4 Complete OC4 5MW FOWT

Considering the contribution of platform, wind turbine, tower etc., the total mass is 1.4075746×10^7 kg, the CoM position is $(0\,\mathrm{m}, 0\,\mathrm{m}, -9,.89\,\mathrm{m})$, and the moment of inertia for roll (I_{xx}), pitch (I_{yy}) and yaw (I_{zz}) are 1.0711×0^{10} kg·m^2, 1.071×10^{10} kg·m^2 and 1.226×10^{10} kg·m^2.
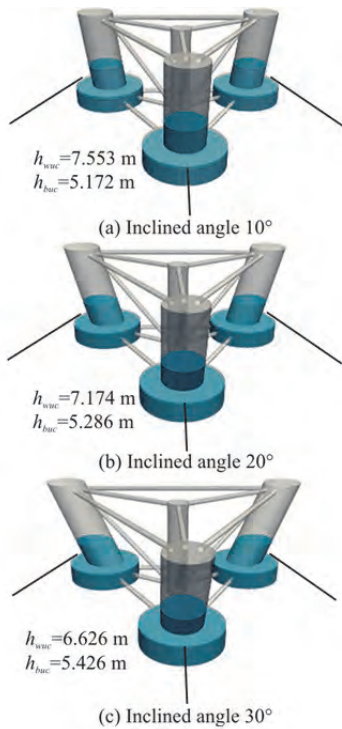

Fig. 7 (Color online) Geometric modeling and ballast water layout

2.2 *New FOWT model with inclined angle*

In this study, there are three new platform models whose upper column will be inclined with 10°, 20° and 30°, modified from original OC4 platform. The wall thickness of each component keeps the same as OC4

design. Besides, in order to maintain CoM being similar to the original platform with installed superstructure equipment, the ballast water height h_{wuc}, h_{buc} have been adjusted, as showing in Fig. 7. This adjustment method has also been proposed in Ref. [29]. Thus, the total mass for 10°, 20° and 30° are 1.4175×10^7 kg, 1.4425×10^7 kg, 1.4868×10^7 kg, the total CoM for all are 9.89 m, and the moment of inertia (I_{xx}, I_{yy}, I_{zz}) are $(1.1388\times10^{10}$ kg·m^2, 1.1388×10^{10} kg·m^2, 1.2775×10^{10} kg·m^2), $(1.1791\times10^{10}$ kg·m^2, 1.1791×10^{10} kg·m^2, 1.355×10^{10} kg·m^2), $(1.2409\times10^{10}$ kg·m^2, 1.2409×10^{10} kg·m^2, 1.4736×10^{10} kg·m^2).

2.3 *Case conditions*

This paper conducts integrated performance analysis for 2 cases: Regular and irregular condition. The regular wave height is 7.58 m, and the wave period is 9.8 s. The irregular wave significant wave height is 8.1 m, and the spectral peak period is 10.5 s. Within the frequency between 0.03 Hz and 0.387 Hz, there are 128 seeds spacing equally.

For the incoming wind speed, the exponential model is used to define on the inlet boundary

$$U_z = U_0 \left(\frac{z}{H_0}\right)^{0.143} \tag{17}$$

where H_0 means shear wind height, equal to the height of wind turbine, $H_0 = 90$ m in this paper, U_0 means the shear wind speed at $z = H_0$.

The simulation time for regular wave condition is 400 s, above wind turbine rotating 80 revolutions. While for the irregular wave condition, 50 s more than previous one.
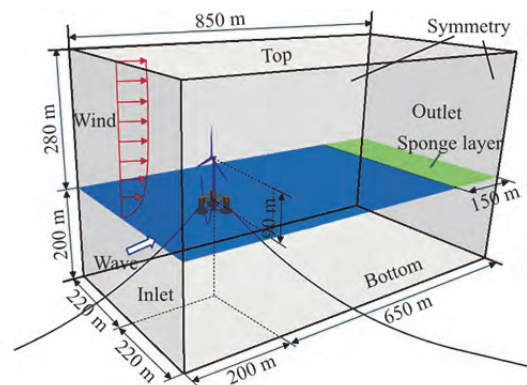

Fig. 8 (Color online) Simulation domain

2.4 *Simulation domain*

For displaying the wake development of wind turbine better, the numerical simulation domain size is

Table 4 Different mesh distributions for validations

Case	Δx (near inlet)/m	Δx (near FOWT)/m	Δz /m
Coarse_x	2.60 $(\lambda/58)$	1.67 $(\lambda/89)$	0.50 $(H/15)$
Medium	1.98 $(\lambda/76)$	1.18 $(\lambda/127)$	0.50 $(H/15)$
Fine_x	1.26 $(\lambda/119)$	1.06 $(\lambda/141)$	0.50 $(H/15)$
Coarse_z	1.98 $(\lambda/76)$	1.18 $(\lambda/127)$	0.71 $(H/11)$
Fine_z	1.98 $(\lambda/76)$	1.18 $(\lambda/127)$	0.38 $(H/20)$

Table 5 The errors between different mesh distributions

Case	Equilibrium position/m	Errors/%	Wave height/m	Errors/%
Theory	0.6073	-	7.580	-
Coarse_x	0.8113	2.69	7.105	6.27
Medium	0.8476	3.17	7.410	2.24
Fine_x	0.8851	3.66	7.450	1.72
Coarse_z	0.8147	2.74	7.403	2.34
Fine_z	0.8466	3.15	7.431	1.96

$x \times y \times z = 850 \text{ m} \times 440 \text{ m} \times 480 \text{ m}$. The OC4 platform is 200 m away from the inlet boundary, the height from the bottom to the water free surface is 200 m, the distance between the left and right sides and the CoM of platform is 220 m, and the length of sponge layer is 150 m, as shown in Fig. 8.

The direction of wave and wind points from the inlet boundary to outlet. The boundary condition at inlet is utilizing the wave making module in our solver, which is achieved by defining velocity and pressure. The outlet boundary condition is zeroGradient, both two sides are symmetry planes. The top boundary uses pressure outlet condition, and the bottom is a slip boundary.

3. Validation for mesh distribution

3.1 *Validation in wave generation*

In order to guarantee the grid near the free surface simulating the preset wave, conduct analysis for the grid convergence for wave generation and determine an appropriate mesh distribution, taking the plane of yoz section in simulation domain for two-dimensional calculation. Different strategies of mesh distribution for validation test are listed in Table 4, which discuss the grids of Δx and Δz, separately. And a variable refinement strategy is adopted in the x-direction, with sparse grids near the inlet boundary and dense grids near the FOWT. In this table, λ is the length of regular wave, H is the wave height.

Simulating by our solver, Fig. 9 displays the wave elevation (η) of wave gauge at $(0,0,0)$ point. Figure 9(a) is the validation for x-direction, and Fig. 9(b) is for z-direction. Only comparing the data after wave simulation stability, it is shown that the differences for wave height (H) between different mesh resolutions significantly decreases with the grid density increasing. Table 5 lists the errors between the nume-

rical and theoretical values, dividing the difference by the theoretical wave height. The monitoring data of medium mesh is only lower than the theory 2.24%. From Fig. 9 and Table 5, we can conclude that the medium grid mesh can meet the wave generation requirements. Especially for z-direction, there is basically no difference in these three gird densities.
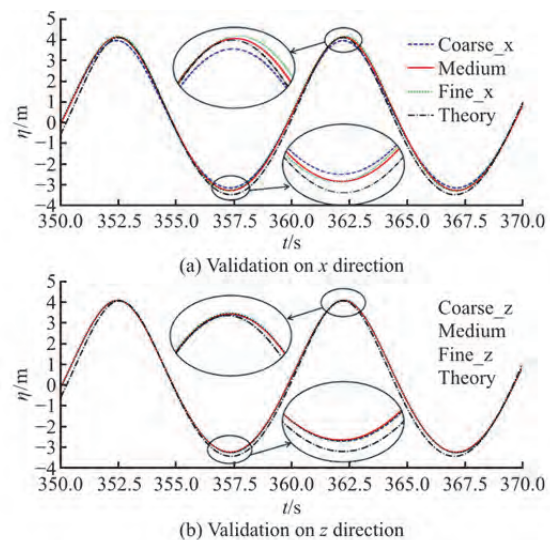

Fig. 9 (Color online) Wave elevation of different mesh distributions

3.2 *Validation in wind generation*

Using the medium mesh distribution strategy to simulate, Fig. 10 shows the average wind speed distribution on a straight line along z-direction, at $x = 126 \text{ m}$, $y = 0 \text{ m}$, from 350 s to 400 s. The vertical axis is the height above sea level. The wind speed profile of numerical simulation remains basically consistent with the standard exponential model.

3.3 *Mesh distribution*

Using the medium distribution strategy, the grid

distribution of simulation is shown in Fig. 11. The total grid number is about 4.02×10^6.
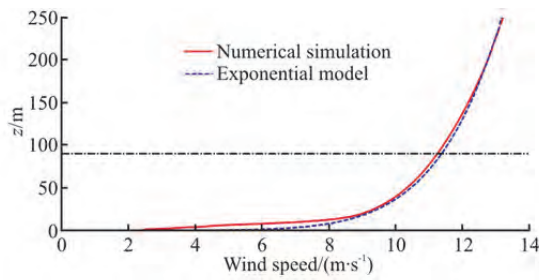

Fig. 10 (Color online) Wind speed profile
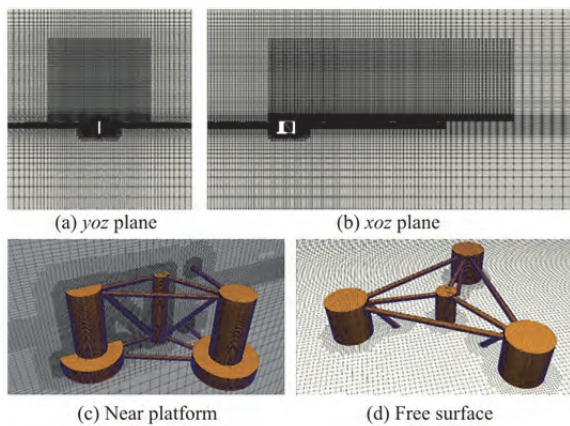

(a) *yoz* plane   (b) *xoz* plane

(c) Near platform   (d) Free surface

Fig. 11 (Color online) Grid of simulation

4. Results and analysis

4.1 *Hydrodynamic motion response*

4.1.1 Regular wave

Figure 12 shows four FOWT types hydrodynamic motion response after approaching stability in regular wave condition. Due to the wave propagation direction, only surge, heave, and pitch motion response amplitudes are significant, constituting the primary focus. Form the Figs. 12(a), 12(e), it is shown directly that with the increase of inclined angles, the equilibrium position of surge is constantly rising, while pitch is decreasing. Which indicates that tilting the column would result in an increase of hydrodynamic force acting on the platform under wave condition. Although this has negative impact on the translational motion of floating platform, it will improve the buoyancy in inclined state. That's also the reason why in Fig. 12(d), the heave motion amplitude increases with inclined angle.

In order to better compare the trends of motion changes, the average amplitude and equilibrium position of the last 50 s are given in Tables 6(a)-6(c). Due
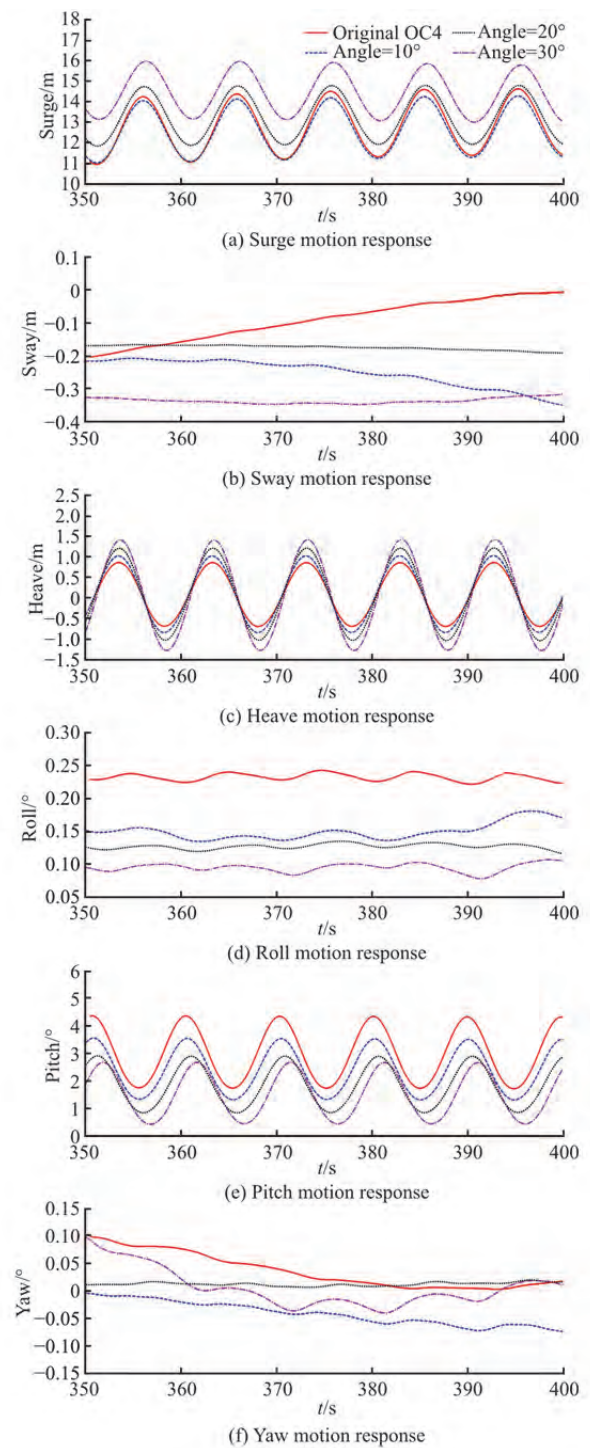

Fig. 12 (Color online) Motion response in regular wave

to the equilibrium position of heave motion nearly $z = 0$, the differences between FOWT models are ignored. The model of inclined 30° angle could decrease the pitch motion equilibrium position and amplitude 49.83%, 15.15% compared with original OC4 FOWT. Which means reducing the peak of pitch motion from 4.326° to 2.628°, in the stable state, nearly

Table 6(a) The equilibrium position and average amplitude of surge motion response

Case	Equilibrium position/m	Difference/%	Average amplitude/m	Difference/%
Original OC4	12.625	-	1.626	-
Angle = 10°	12.787	1.28	1.840	13.16
Angle = 20°	13.292	5.28	1.477	−9.16
Angle = 30°	14.459	14.53	1.482	−8.86

Table 6(b) The equilibrium position and average amplitude of heave motion response

Case	Equilibrium position	Difference/%	Average amplitude/m	Difference/%
Original OC4	0.0766 m	-	0.7800	-
Angle 10°	0.0836 m	9.14	0.9400	20.51
Angle 20°	0.0821 m	7.18	1.1295	44.81
Angle 30°	0.0573 m	−25.2	1.3605	74.42

Table 6(c) The equilibrium position and average amplitude of pitch motion response

Case	Equilibrium position/°	Difference/%	Average amplitude/°	Difference/%
Original OC4	3.006	-	1.320	-
Angle = 10°	2.390	−25.52	1.120	−15.15%
Angle = 20°	1.837	−38.89	1.032	−21.82%
Angle = 30°	1.508	−49.83	1.120	−15.15%

Table 7(a) Statistical value of rotor power (MW)

Case	Mean	rms	Max	Min	Amp	STD
Original OC4	5.083	5.103	5.980	4.443	1.536	0.444
Angle = 10°	5.097	5.107	5.818	4.652	1.166	0.319
Angle = 20°	5.106	5.110	5.609	4.675	0.935	0.202
Angle = 30°	5.112	5.121	5.578	4.473	1.107	0.296

Table 7(b) Statistical value of rotor thrust (kN)

Case	Mean	rms	Max	Min	Amp	STD
Original OC4	674.06	674.06	719.67	640.34	79.33	23.97
Angle = 10°	676.44	676.66	711.43	652.30	59.14	17.13
Angle = 20°	678.01	678.09	702.13	654.39	47.74	10.77
Angle = 30°	678.61	678.82	700.89	642.09	58.80	17.00

39.25%. However, from the perspective of reducing the amplitude of motion, the angle of 20° is the best choice.

4.1.2 Irregular wave

For the irregular wave, the 6DOF motion response time domain curves are shown in Fig. 13. However, apart from being able to see that the equilibrium position of pitch motion increases with the inclined angle, similar with regular wave cases, it is difficult to visually display other information. Thus, conduct frequency domain analysis for three significant motions (surge, heave, pitch), shown in Fig. 14.

Those power spectrum density figures in indicate which components have the greatest impact on FOWT motion oscillation changes. The gray region represents the wave generated frequency input, and bule region covers the natural frequency of each motion. Besides, $f_p = 0.0952\,\text{Hz}$, is the spectral peak frequency, and $f_{rotor} = 0.2017\,\text{Hz}$ is the rotor rotating frequency. For surge motion in Fig. 14(a), there are two distinct peaks appearing near the natural period and spectral peak frequency. Combined with Fig. 13(a), the free decay of platform plays an important role in surge motion response. Next is the impact of waves. The rotor almost

only provides thrust in x-direction. However, for the heave and pitch motion, the rotor rotating frequency shows more importance. Even near $2f_{rotor}$, it occurs strong oscillations. Besides, it can be observed that the natural frequency of pitch would increase with inclined angle, as shown in the blue region of Fig. 14(e). Thus, it is so important to pay attention to the changes in natural frequency (period) caused by structural changes and avoid them falling near the peak frequency as possible.

4.2 Aerodynamic performance

4.2.1 Regular wave

The curve of rotor power and thrust in last simulated 50 s are shown in Fig. 15, which indicates that the power and thrust will also exhibit periodic fluctuations in regular waves. Directly, with the increase of inclined angle, there are two peak points shown within a periodic variation, and the value of second peak gradually increases. The first peak value circled in Fig. 15 occurs near 382s, which is close to the occurrence time of peak pitch motion in Fig. 12(e). While, for the second peak, it is related to the heave motion. Due to
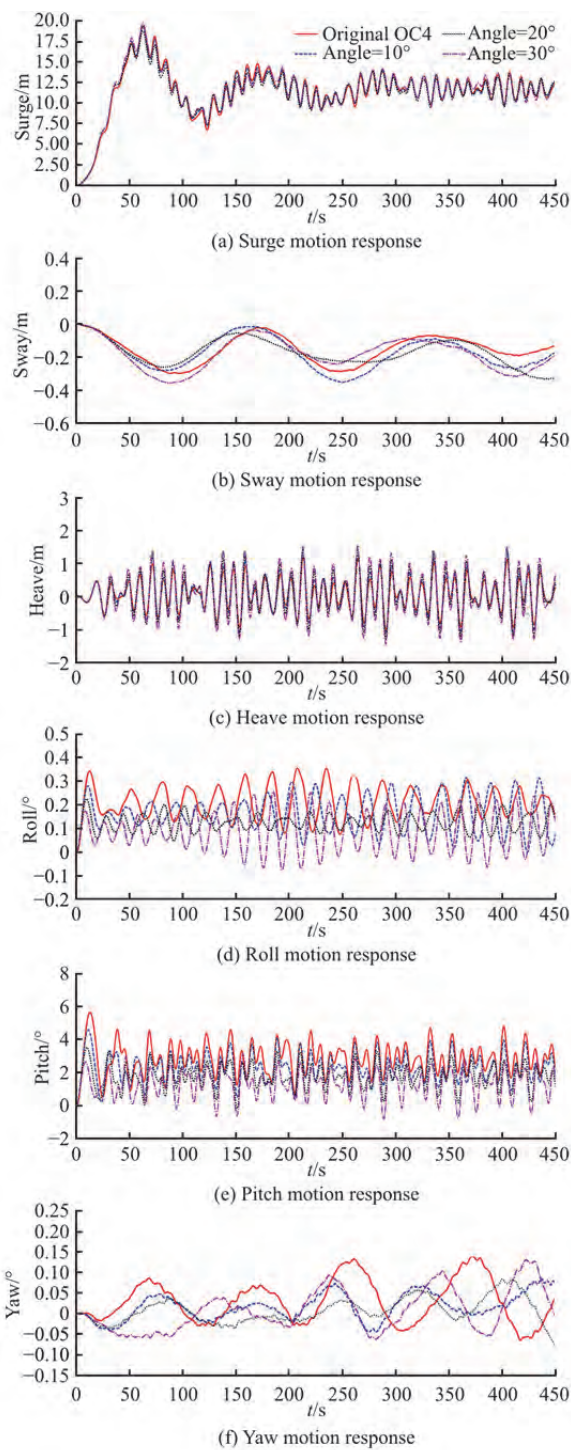
Fig. 13 (Color online) Motion response in irregular wave

the increase in inclined angles, the platform's heave motion amplitude increases, which would result in the increase of motion velocity, either. The second peak value circled in Fig. 15 appears around 388 s, close to the moment when heave motion is at the equilibrium position and also the moment of maximum heave velocity.
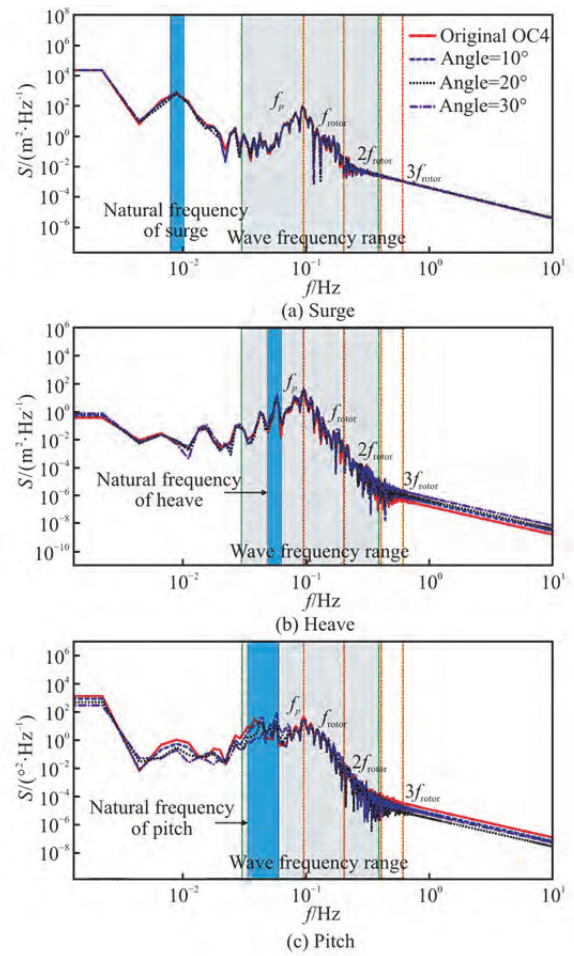

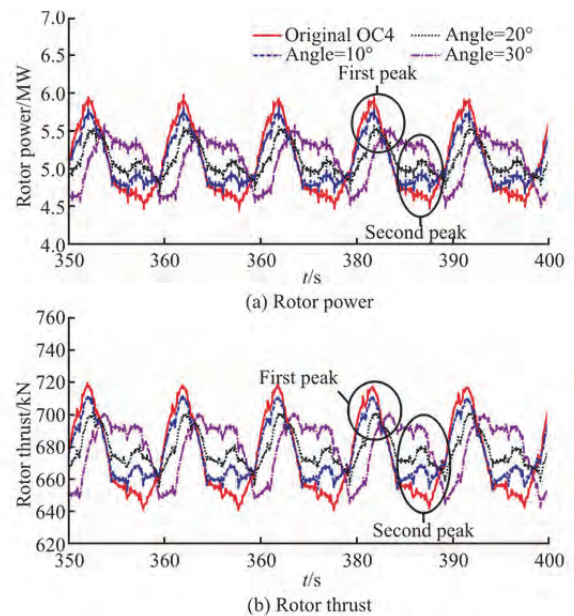Fig. 14 (Color online) Power spectrum density of motion response

Fig. 15 (Color online) Rotor power and thrust in regular wave
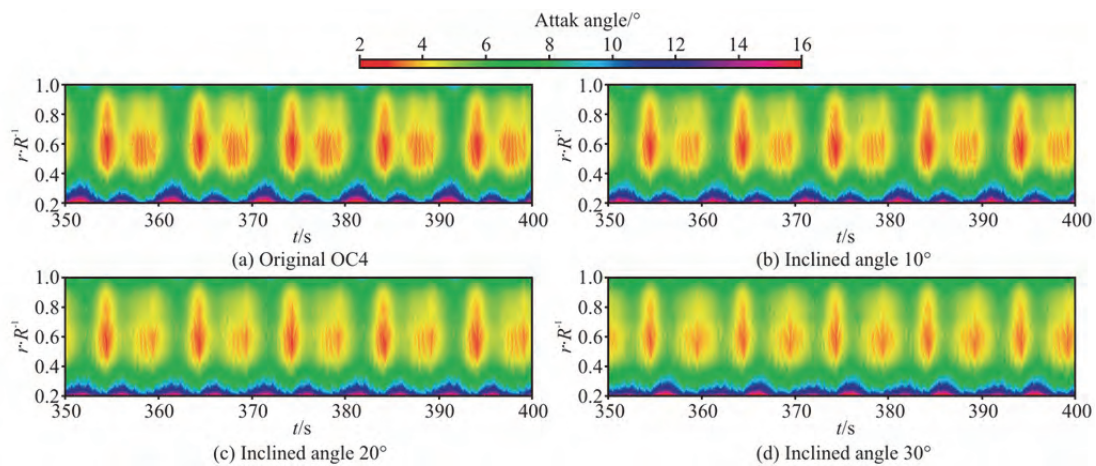
Springer

Fig. 16 (Color online) The variation curve of attack angel along the spanwise
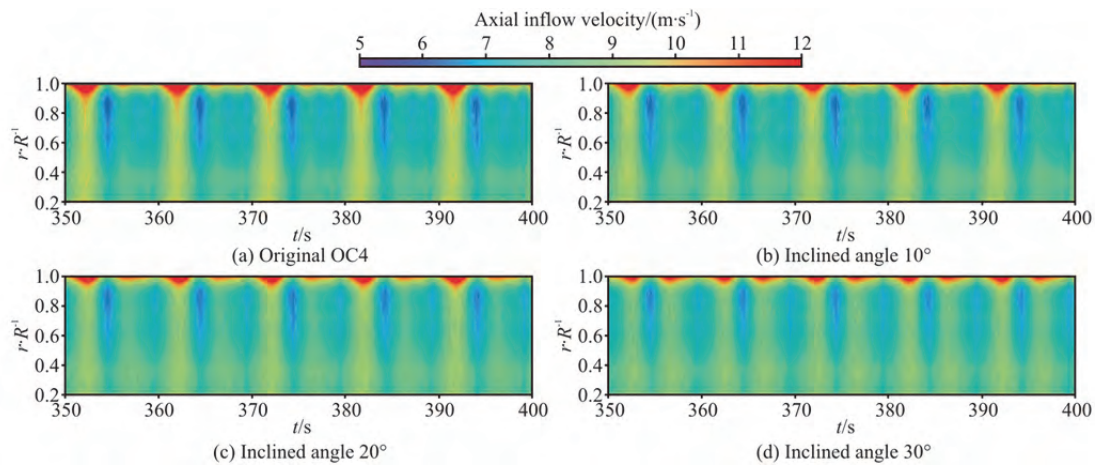

Fig. 17 (Color online) The variation curve of axial inflow velocity along the spanwise

Tables 7(a), 7(b) lists the statistical value of curves in Fig. 15. Whether it is mean or root mean square (rms) value of power and thrust, it is growing up with inclined angle. The rms of power and thrust increase 0.35%, 0.71% when inclined angle = 30°. However, for the amplitude and standard deviation (STD) value the minimum appears at the angle equal to 20°. The STD in power and thrust decrease 33.33%, 55.07%. Although the effect of inclined angle on average power is relatively small, it can significantly reduce the amplitude variation range, reduce the maximum loads, and improve the structural safety.

This bimodal phenomenon of aerodynamic loads could be well explained by variation in the attack angle and axial inflow velocity, as shown in Figs. 16, 17. With the inclined angles increasing, there are two low regions of attack angle and high regions of axial inflow velocity appearing from 380 s to 390 s, corresponding to the two peaks in aerodynamic loads. Additionally, it can be observed that, with the increase of inclined angle, the red high-velocity region contracts. This is one of the most important reason for the decreases in the aerodynamic loads peak value at the first peak position in Fig. 15.

4.2.2 Irregular wave

Figure 18 shows the rotor power and thrust in irregular wave, and Tables 8(a), 8(b) lists the statistical value. Different from the regular wave, although the rms value of power and thrust are growing up with inclined angle, the maximum value also increases. Besides, the minimum value of STD and amplitude appears in angle 10°. Compared with the original OC4 model, for the inclined angle = 10° the rms value of power only increases 0.8%, the rms value of thrust increases 0.26%. And the STD values decrease 3.85%, 4%. However, for the inclined angle = 30°, the STD values increase 57.09%, 60.56%. Thus, it is worth noting that the true sea state is a more complex calculation condition, and the local real sea conditions must be simulated if FOWT optimized.

Table 8(a) Statistical value of rotor power (MW) under irregular wave condition

Case	Mean	rms	Max	Min	STD
Original OC4	5.091	5.115	6.023	3.799	0.494
Angle = 10°	5.099	5.121	6.119	3.854	0.475
Angle = 20°	5.113	5.140	6.280	3.877	0.523
Angle = 30°	5.124	5.183	6.765	3.128	0.776

Table 8(b) Statistical value of rotor thrust (kN) under irregular wave condition

Case	Mean	rms	Max	Min	STD
Original OC4	675.04	675.63	726.05	596.06	28.12
Angle = 10°	676.83	677.36	730.56	602.24	27.00
Angle = 20°	678.16	678.82	739.31	601.64	29.90
Angle = 30°	677.79	679.29	762.74	548.69	45.15

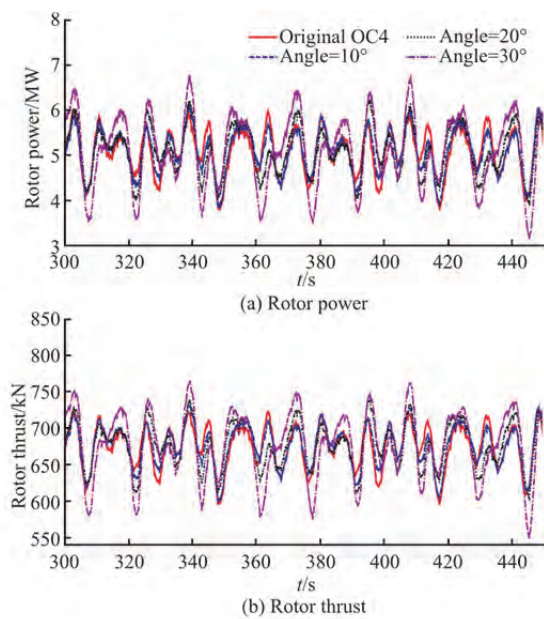

Fig. 18 (Color online) Rotor power and thrust in irregular wave

4.3 *Wind turbine wake flow recovery*

In order to analyze the wake characteristics of wind turbines, the velocity field for the latest 100 s under irregular wave condition is time-averaged. Figure 19 displays the color map of wake velocity deficit on the $z = 90\,\mathrm{m}$ plane with different inclined column angles. Where, the coordinate axes are normalized by the rotor plane diameter, $D = 126\,\mathrm{m}$. Δu is the difference between time-mean velocity $\overline{U_x}$ and inflow wind speed $U_{\mathrm{wind}} = 11.4\,\mathrm{m/s}$, $\Delta u = U_{\mathrm{wind}} - \overline{U_x}$.

Data are extracted from each $x = 1.0D$ position in Fig. 19 to obtain the wake deficit profiles, as shown in Fig. 20. It can be observed that with the wake developing downstream, the velocity deficit around wake center ($y = 0D$, approximately) gradually increases, under the recovery effects from both wake

sides. Additionally, in the range of $x = 3.0D\text{-}5.0D$, affected by the platform motion, the curve with a larger inclined angle would be closer to the left, especially on the wake center. Which means the recovery of FOWT wake with inclined angle will become faster.

Try to study the recovery of velocity in the middle to far wake region, Fig. 21 shows the time-mean velocity at the $x = 3.0D$, $4.0D$ and $5.0D$ sections. The origin coordinate axes of those figures are located at the center of rotor plane (black dot), i.e., $y = 0\,\mathrm{m}$, $z = 90\,\mathrm{m}$ in simulation domain. And the black circles represent rotor plane. In terms of wake development, as the wake extends downstream, the velocity deficit gradually recovers, the central velocity decreases, and its position shifts upward. In terms of the effect of inclined column angles, the FOWT with a larger inclined angle has a greater wake velocity near the free surface, which means more recovery of the downstream wake. The FOWT model with inclined columns is meaningful for the design and construction of floating offshore wind farms, as it can enhance the inflow wind energy for downstream turbines.

5. Conclusions

In this study, four FOWT types with different inclined column angles are taken into account by using our in-house CFD solver FOWT-UALM-SJTU. The validation in wave and wind making is conducted to determine the strategy of mesh distribution. Under two conditions of regular and irregular waves, the 6DOF hydrodynamic motion responses, aerodynamic performance and the wake development are analyzed to explore the impact of inclined angle. Several conclusions like that:

(1) Under regular wave condition, with the increase of inclined angles, the equilibrium position of surge motion is constantly rising, while pitch is decreasing. The model of inclined angle is 30° could decrease 49.83% of the pitch motion equilibrium position and 15.15% of amplitude. However, heave motion amplitude shows the phenomenon of increasing with inclined angle. From the spectral analysis of motion responses under irregular wave, it is indicated that the platform motion is mainly manifested as wave frequency motion, while the surge is mainly based on the natural frequency. Besides, the natural frequency of
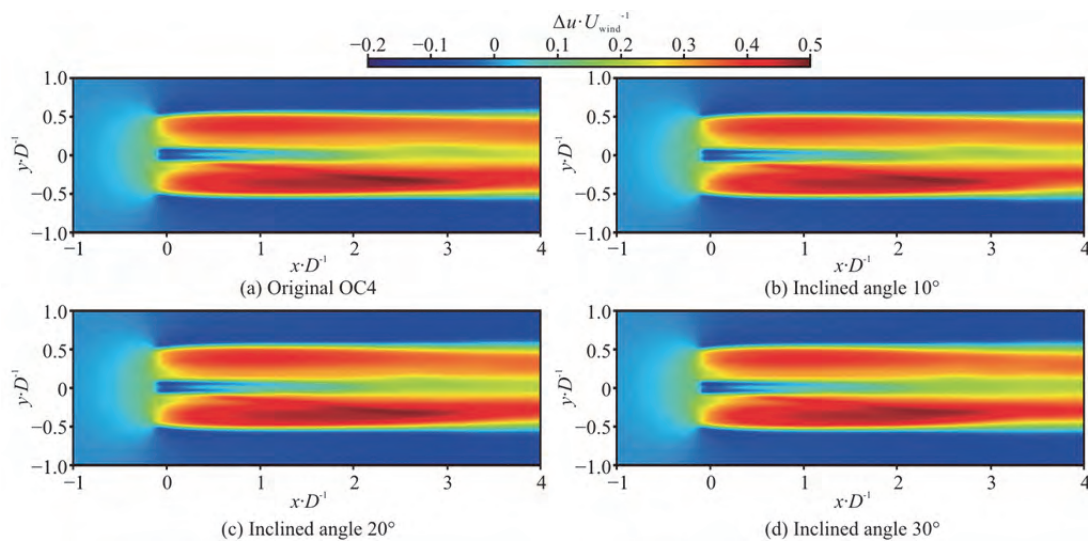
Fig. 19 (Color online) Color map of the wake velocity deficit on $z = 90\,\mathrm{m}$ plane with different inclined column angles
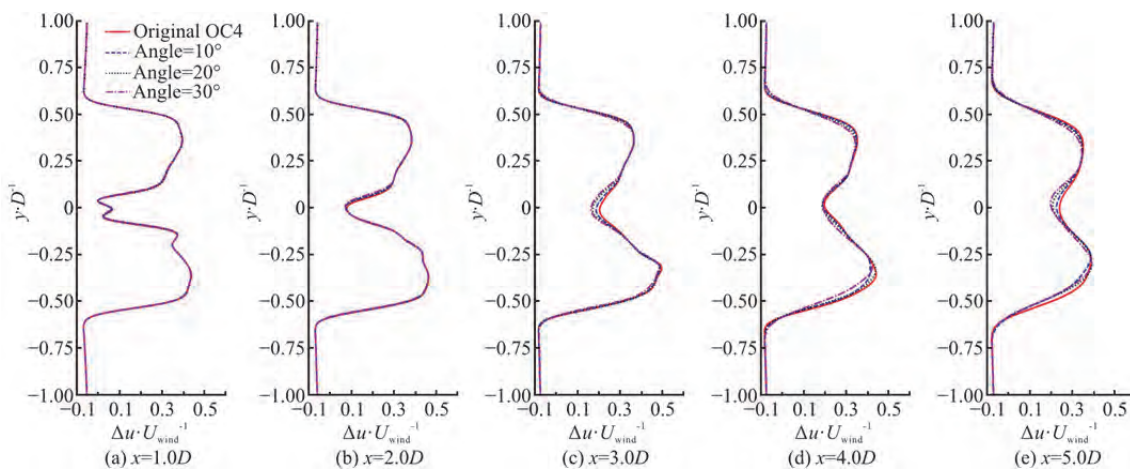

Fig. 20 (Color online) Curves of the wake velocity deficit profile

pitch motion will increase with angle enlarge. It is very important to pay attention to the natural frequency (period) changes caused by structural changes and avoid them falling near the wave crest as much as possible.

(2) For the aerodynamic rotor power and thrust, although the rms, STD values do not always vary with the inclined angle for different conditions, increasing the inclined angle still effectively improves the aerodynamic performance. The maximum rms values occur at angle is 30°, and the rms in power and thrust increase 0.35%, 0.71%, under regular wave condition. Additionally, with the inclined angles increasing, there are two low regions of attack angle and high regions of axial inflow velocity, also expressed in the aerodynamic loads. Under irregular wave condition, the rms value increase 1.33%, 0.54%. However, the minimum STD appears at 20°, 10° for regular and

irregular wave condition. The STD value decrease 33.33%, 55.07% in regular wave when angle is 20°, and decrease 3.85%, 4.00% in irregular wave when angle is 10°.

(3) With the wake developing downstream, the velocity deficit around wake center will increase gradually, and its position shifts upward. While the velocity deficit would recover surrounding the center. Besides, in the middle to far regions of wake, the recovery of FOWT wake with inclined angle will become faster, especially near the free surface. It is beneficial for downstream turbines to enhance more wind energy, and meaningful for floating offshore wind farms designs and distributions.

In this study, although conducted on two different conditions and four types FOWT, the results indicate that increasing the inclined angle could reduce the hydrodynamic motion response, improve the
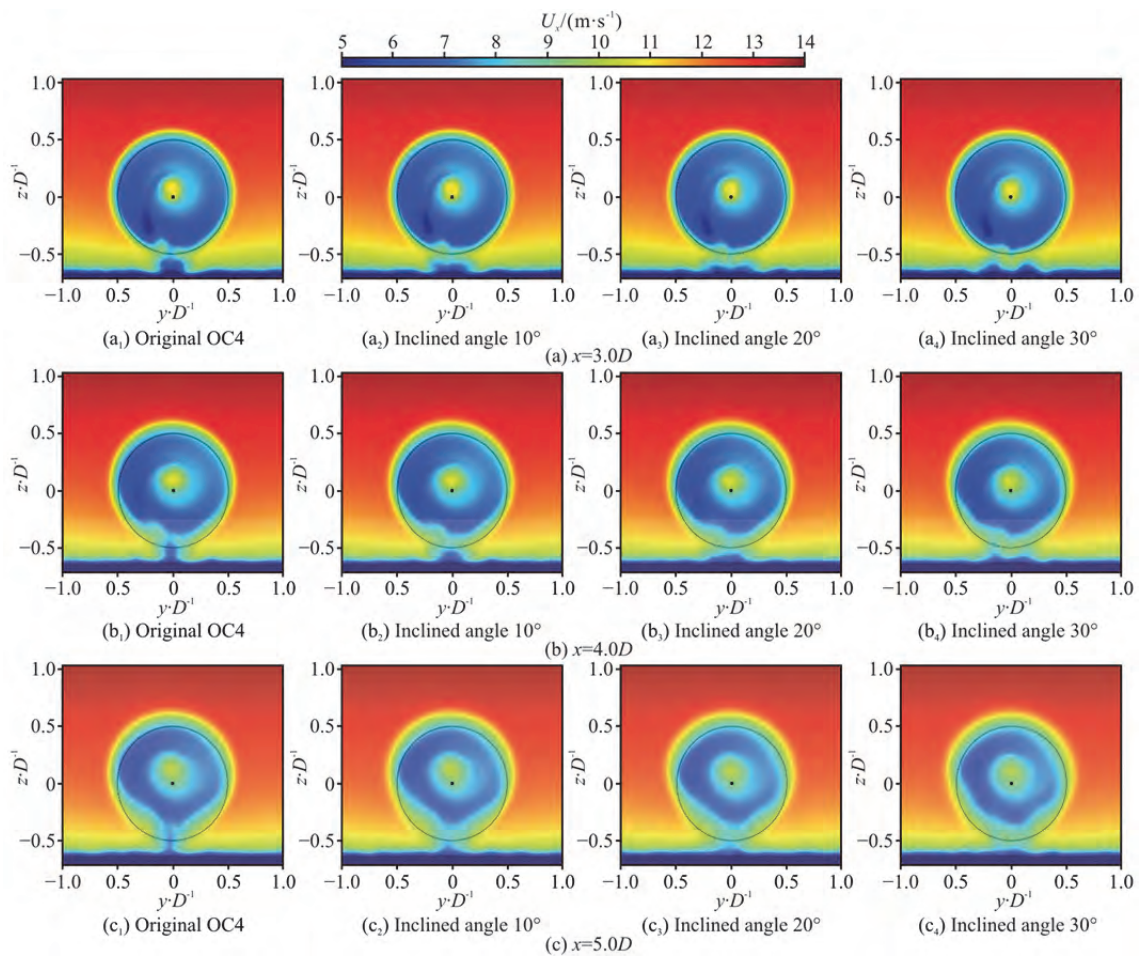
Fig. 21 (Color online) Time-mean wake velocity at different downstream sections

aerodynamic rotor power, promote the wake recovery, more conditions should be calculated if used for true design. Besides, more design parameters need to be considered when optimizing the design of floating platforms.

Acknowledgement

Compliance with ethical standards

Conflict of interest: The authors declare that they have no conflict of interest. De Cheng-Wan is editorial board member for the Journal of Hydrodynamics and was not involved in the editorial review, or the decision to publish this article. All authors declare that there are no other competing interests.

Ethical approval: This article does not contain any studies with human participants or animals performed by any of the authors.

Informed consent: Not application.

References

[1] Joselin Herbert G. M., Iniyan S., Sreevalsan E. et al. A review of wind energy technologies [J]. *Renewable and Sustainable Energy Reviews*, 2007, 11(6): 1117-1145.

[2] Blanco M. I. The economics of wind energy [J]. *Renewable and Sustainable Energy Reviews*, 2009, 13(6): 1372-1382.

[3] Esteban M. D., Diez J. J., López J. S. et al. Why offshore wind energy? [J]. *Renewable Energy*, 2011, 36(2): 444-450.

[4] Roga S., Bardhan S., Kumar Y. et al. Recent technology and challenges of wind energy generation: A review [J]. *Sustainable Energy Technologies and Assessments*, 2022, 52: 102239.

[5] Global Wind Energy Council. GWEC | Global wind report 2023 [R]. Brussels, Belgium: Global Wind Energy Council, 2023.

[6] Xu S., Xue Y., Zhao W. et al. A review of high-fidelity computational fluid dynamics for floating offshore wind turbines [J]. *Journal of Marine Science and Engineering*, 2022, 10(10): 1357.

[7] Ke S., Yu W., Cao J. et al. Aerodynamic force and comprehensive mechanical performance of a large wind turbine during a typhoon based on WRF/CFD nesting [J].

Applied Sciences-Basel, 2018, 8(10): 1982.

[8] Ojo A., Collu M., Coraddu A. Multidisciplinary design analysis and optimization of floating offshore wind turbine substructures: A review [J]. *Ocean Engineering*, 2022, 266: 112727.

[9] Sclavounos P., Tracy C., Lee S. Floating offshore wind turbines: Responses in a seastate pareto optimal designs and economic assessment [C]. *Proceedings of the ASME 27th International Conference on Offshore Mechanics and Arctic Engineering*, Estoril, Portugal, 2008.

[10] Tracy C. C. H. Parametric design of floating wind turbines [D]. Doctoral Thesis, Cambridge, USA: Massachusetts Institute of Technology, 2007.

[11] Yang Y., Bashir M., Michailides C. et al. Development and application of an aero-hydro-servo-elastic coupling framework for analysis of floating offshore wind turbines [J]. *Renewable Energy*, 2020, 161: 606-625.

[12] Zou Q., Lu Z., Shen Y. Short-term prediction of hydrodynamic response of a novel semi-submersible FOWT platform under wind, current and wave loads [J]. *Ocean Engineering*, 2023, 278: 114471.

[13] Brommundt M., Krause L., Merz K. et al. Mooring system optimization for floating wind turbines using frequency domain analysis [J]. *Energy Procedia*, 2022, 24: 289-296.

[14] Zhao Z., Shi W., Wang W. et al. Dynamic analysis of a novel semi-submersible platform for a 10 MW wind turbine in intermediate water depth [J]. *Ocean Engineering*, 2021, 237: 109688.

[15] Liu S., Chuang Z., Wang K. et al. Structural parametric optimization of the VolturnUS-S semi-submersible foundation for a 15 MW floating offshore wind turbine [J]. *Journal of Marine Science and Engineering*, 2022, 10(9): 1181.

[16] Karimi M., Hall M., Buckham B. et al. A multi-objective design optimization approach for floating offshore wind turbine support structures [J]. *Journal of Ocean Engineering and Marine Energy*, 2017, 3(1): 69-87.

[17] Hall M., Buckham B., Crawford C. Evolving offshore wind: A genetic algorithm-based support structure optimization framework for floating wind turbines [C]. *2013 MTS/IEEE OCEANS-Bergen*, Bergen, Norway, 2013.

[18] Hegseth J. M., Bachynski E. E., Martins J. R. R. A. Integrated design optimization of spar floating wind turbines [J]. *Marine Structures*, 2020, 72: 102771.

[19] Halfpenny A. A frequency domain approach for fatigue life estimation from finite element analysis[J]. *Key Engineering Materials*, 1999, 167: 401-410.

[20] Robertson A., Jonkman J., Masciola M. et al. Definition of the semisubmersible floating system for phase II of OC4 [R]. Golden, USA: National Renewable Energy Laboratory, 2014.

[21] Jonkman J., Butterfield S., Musial W. et al. Definition of a 5-MW reference wind turbine for offshore system development [R]. Golden, USA: National Renewable Energy Laboratory, 2009.

[22] Coulling A. J., Goupee A. J., Robertson A. N. et al. Validation of a FAST semi-submersible floating wind turbine numerical model with DeepCwind test data [J]. *Journal of Renewable and Sustainable Energy*, 2013, 5: 023116.

[23] Tran T. T., Kim D-H. The coupled dynamic response computation for a semi-submersible platform of floating offshore wind turbine [J]. *Journal of Wind Engineering and Industrial Aerodynamics*, 2015, 147: 104-119.

[24] Cheng P., Huang Y., Wan D. A numerical model for fully coupled aero-hydrodynamic analysis of floating offshore wind turbine [J]. *Ocean Engineering*, 2019, 173: 183-196.

[25] Ferri G., Marino E., Borri C. Optimal dimensions of a semisubmersible floating platform for a 10 MW wind turbine [J]. *Energies*, 2020, 13(12): 3092.

[26] Ferri G., Marino E., Bruschi N. et al. Platform and mooring system optimization of a 10 MW semisubmersible offshore wind turbine [J]. *Renewable Energy*, 2022, 182: 1152-1170.

[27] Liu Z., Zhou Q., Tu Y. et al. Proposal of a novel semi-submersible floating wind turbine platform composed of inclined columns and multi-segmented mooring lines [J]. *Energies*, 2019, 12(9): 1809.

[28] Zhang H., Wang H., Cai X. et al. Research on the dynamic performance of a novel floating offshore wind turbine considering the fully-coupled-effect of the system [J]. *Journal of Marine Science and Engineering*, 2022, 10(3): 341.

[29] Xue Y., Zhang X., Wan D. Numerical study of the effect of inclined columns on the performance of floating offshore wind turbine platform [C]. *The 10th International Conference on Computational Methods in Marine Engineering*, Madrid, Spain, 2023.

[30] Huang Y., Zhao W., Wan D. Wake interaction between two spar-type floating offshore wind turbines under different layouts [J]. *Physics of Fluids*, 2023, 35: 097102.

[31] Zheng J., Wang N., Wan D. et al. Numerical investigations of coupled aeroelastic performance of wind turbines by elastic actuator line model [J]. *Applied Energy*, 2023, 330: 120361.

[32] Cao H., Wan D. Development of multidirectional non-linear numerical wave tank by Naoe-FOAM-SJTU solver [J]. *International Journal of Ocean System Engineering*, 2014, 4(1): 49-56.

[33] Wang J. H., Zhao W. W., Wan D. C. Development of naoe-FOAM-SJTU solver based on OpenFOAM for marine hydrodynamics [J]. *Journal of Hydrodynamics*, 2019, 31(1): 1-20.

[34] Huang Y., Wan D. Investigation of interference effects between wind turbine and spar-type floating platform under combined wind-wave excitation [J]. *Sustainability*, 2020, 12(1): 246-277.

[35] Gritskevich M. S., Garbaruk A. V., Schütze J. et al. Development of DDES and IDDES formulations for the k-ω shear stress transport model [J]. *Flow, turbulence and Combustion*, 2012, 88: 431-449.

[36] Zhao W. W., Meng Q. J., Wan D. C. et al. Vortex structures of dynamic pure yaw test using DDES approach and vortex identification method [J]. *Journal of Hydrodynamics*, 2022, 34(2): 226-233.

[37] Hirt C. W., Nichols B. D. Volume of fluid (VOF) method for the dynamics of free boundaries [J]. *Journal of Computational Physics*, 1981, 39(1): 201-225.

[38] Fenton J. D. A fifth-order Stokes theory for steady waves [J]. *Journal of* Waterway, *Port, Coastal, and Ocean Engineering*, 1985, 111(2): 216-234.

[39] Sørensen J., Shen W. Numerical modeling of wind turbine wakes [J]. *Journal of Fluids Engineering*, 2002, 124(2): 393-399.